



# Enhanced dynamic landslide hazard mapping using MT-InSAR method in the Three Gorges Reservoir Area

**Abstract** Landslide hazard mapping is essential for disaster reduction and mitigation. The hazard map produced by the spatiotemporal probability analysis is usually static with false-negative and false-positive errors due to limited data resolution. Here we propose a new method to obtain dynamic landslide hazard maps over the Wushan section of the Three Gorges Reservoir Area by introducing the ground deformation measured by the spaceborne Copernicus Sentinel-1 synthetic aperture radar (SAR) imagery collected from 9/30/2016 to 9/13/2017. We first determine the spatial probability of landslide occurrence predicted by the support vector machine algorithm. We also conducted the statistical analysis on the temporal probability of landslide occurrence under various rainfall conditions (0, 0–50, 50–100, and >100 mm for the antecedent 5-day total). We initialize a preliminary landslide hazard map by combining the spatial and temporal landslide probabilities. Meanwhile, the ground deformation velocities during the representative dry and wet seasons can be extracted from multi-temporal interferometric SAR (MT-InSAR). Thereafter, the landslide hazard map can be finalized by an empirical assessment matrix considering both the preliminary landslide hazard map and deformation velocities. Our results demonstrate that false-negative and false-positive errors in the landslide hazard map can be effectively reduced with the assistance of the deformation information. Our proposed method can be used to assess the dynamic landslide hazard at higher accuracy.

**Keywords** Landslide · MT-InSAR · Dynamic hazard mapping · Three Gorges Reservoir Area

## Introduction

Landslides are common natural hazards that pose threats to the life and property worldwide (Froude and Petley 2018). In particular, the Three Gorges Reservoir Area (TGRA) in China is vulnerable to mass wasting due to fragile geological conditions, seasonal rainfall, and drastic reservoir filling (Tang et al. 2019; Cao et al. 2020). More than 5000 landslides over TGRA directly put critical lifelines and transportation corridors at risks. Landslide hazard mapping aims to quantify the spatial and temporal probabilities of landslides (Segoni et al. 2018). Knowledge on the geographic locations and timing of landslides is essential to natural hazard reduction and mitigation.

Landslide susceptibility is the spatial probability of landslide occurrence based on a group of predisposing factors (such as slope, lithology) (Van Westen et al. 2003; Guzzetti et al. 2006; Chen et al. 2020, 2021; Hong et al. 2020; Pham et al. 2020). The engineering geological analogy is the theoretical basis of landslide susceptibility

modeling (LSM). It assumes that future landslides are more likely to occur under similar conditions as previous events (Neuhäuser and Terhorst 2007; Zhou et al. 2020a). The data-driven algorithms of LSM such as support vector machine (SVM) (Bui et al. 2012; Pourghasemi et al. 2013; Zhou et al. 2018a), random forest (Catani et al. 2013; Hong et al. 2019; Wang et al. 2020a, b), logistic regression (Lee and Sambath 2006; Bai et al. 2010), and artificial neural networks (Pradhan and Lee 2010; Gomez and Kavzoglu 2005) have been widely used. The temporal probability of landslide occurrence defines the time and frequency of the slope failures in response to the specific triggering factor, including rainfall and earthquake.

Slow-moving landslides spread over the TGRA. The lifetime of slow-moving landslides transitioning from slow movement to dynamic failures can last for hundreds of years (Lacroix et al. 2020). The slope deformation responds to environmental forces differently during the landslide evolution (Cao et al. 2016; Bontemps et al. 2020). The cumulative displacements in the TGRA present a step-like variation in a single water year (Zhou et al. 2018b). The landslide motions accelerate from April to September due to the rapid decline of reservoir water level and intense rainfall. On the other hand, no apparent motion has been observed from October to March in the following year due to the high stand while stable reservoir water level in dry season. We consider two time spans for landslide hazard mapping in TGRA referring to their distinct hydrological conditions and deformation.

The spatial and temporal probabilities of landslide occurrences have been used to produce hazard maps in landslide-prone areas (e.g., Guzzetti et al. 2005; Kawagoe et al. 2010; Segoni et al. 2014; Fu et al. 2020). However, a lack of knowledge on landslide deformation may lead to misinterpretation. Two types of errors are considered, namely, false-positive and false-negative errors. The false-positive error means that the off-slide terrains are misclassified as unstable slopes. Therefore, the land use of these terrains may be restricted. The false-negative error means that the on-slide terrains are misclassified as stable areas. The consequence of false-negative error can be fatal. When these landslide-affected terrains are developed without caution, Catastrophic consequences may be triggered by persistent creep or dynamic failures (Corominas et al. 2014; Ciampalini et al. 2016).

Elimination of both types of errors is a priority in landslide hazard reduction. Multi-temporal (MT) Interferometric Synthetic Aperture Radar (InSAR) methods, such as Permanent Scatterer InSAR (PS-InSAR) (Ferretti et al. 2001), Small Baseline Subset (SBAS) (Berardino et al. 2002), and SqueeSAR (Ferretti et al. 2011), have been used to measure spatiotemporal deformation in landslide identification and monitoring (e.g., Lu et al. 2014; Dong et al.

2018; Intrieri et al. 2019; Dai et al. 2020; Hu et al. 2020; Xie et al. 2020; Zhang et al. 2020; Zhou et al. 2020a, b; Bekaert et al. 2020; Wasowski and Pisano 2020; Liu et al. 2021; Handwerger et al. 2021). The contemporary Copernicus Sentinel-1 satellite constellation launched by the European Space Agency (ESA) provides a considerable free collection of SAR imagery for performing MT-InSAR.

The Wushan section of TGRA is subjected to landslides and no hazard map is available. The current application of InSAR in TGRA is focused on the identification of landslide location and triggering factors. In this study, we produce preliminary landslide hazard maps in different rainfall scenarios considering the spatial and temporal probabilities of landslide occurrence. We divide 1 water year into two periods based on the hydrological conditions and the landslide deformation response. The ground deformation velocities are extracted using MT-InSAR, and incorporated to produce landslide hazard maps using an empirical assessment matrix. With this procedure, we attempt to obtain a dynamic and accurate hazard map by integrating information on ground deformation.

### Study area

Our study area is featured with mountains in the Wushan section of TGRA along the Yangtze River (Fig. 1). It is located at the junction of the Daba Mountain, Wushan Mountain, and Qiyashan Mountain with a complex geologic structure. The secondary fold and fault structures are well developed. The exposed stratum in this area is mainly carbonate rocks with clastic rocks of the Lower Triassic Jialingjiang Formation and the Quaternary deposits.

The study area has a humid subtropical climate with abundant rainfall. The average annual rainfall is 1049 mm. The maximum annual rainfall is 1356 mm and the maximum monthly rainfall is 446 mm in September 1979. The maximum daily rainfall of 385 mm occurred on August 31, 2014. The seasonal rainfall mainly occurs from May to September, accounting for ~ 69% of the annual total (Yu et al. 2019). The reservoir water level of TGRA was initially impounded from 69 to 135 m a.s.l. in 2003. It has been in cyclic hydraulic operation since 2009 with a fluctuation between 145 and 175 m a.s.l. The rapid water level rise and drawdown in the TGRA keep modifying the hydrogeological environment of the reservoir banks and promoting the bank instability.

The gully and hill-cutting landscapes are exposed to frequent landslide disasters (Zhou et al. 2013; Huang et al. 2019; Ahmed 2021). For example, the global dataset of landslide occurrence recorded by Froude and Petley (2018) shows that 11.3% of fatal landslides are caused by illegal hill-cutting between 2004 and 2016. The hydrodynamic pressures and lateral erosions caused by water-level fluctuation mobilize the bank slopes. Based on high-resolution remote sensing imagery, field investigations, and landslide reports, a total of 165 landslides have been included in the landslide inventory (Fig. 1). Most of them are colluvial landslides. They cover an area of  $12.65 \text{ km}^2$ , and individual landslides range between  $1.7 \times 10^{-3}$  and  $1.06 \text{ km}^2$ . Rainfall, water level fluctuations of TGRA, and anthropogenic activities are the main triggering factors of the initiation and deformation of landslides. Among all landslide terrains, fifteen of them are currently unstable.

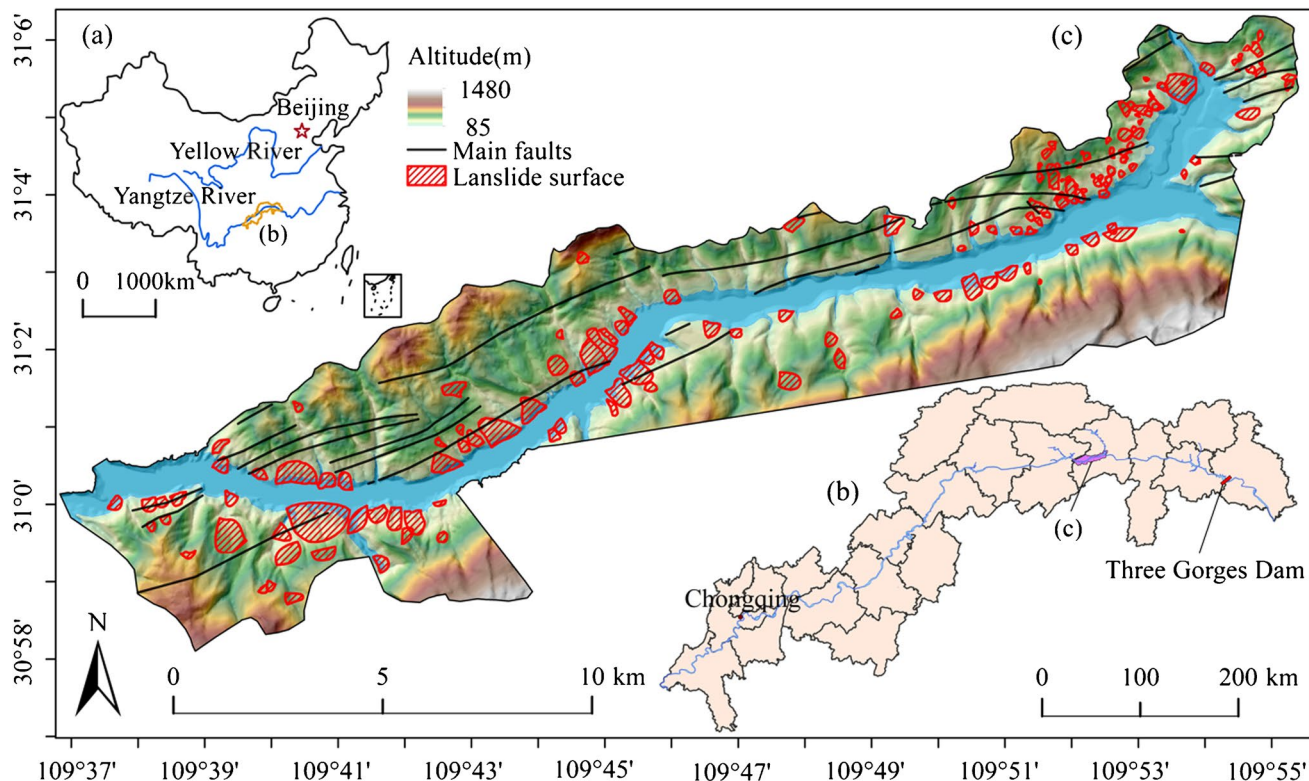


**Fig. 1** **a** Geographic location of our study area. **b** Three Gorges Reservoir Area. **c** Landslides in the Wushan segment marked with the cross-hatched red areas superimposed on the surface elevation

## Methodology

### The principle of landslide hazard mapping

#### Landslide susceptibility modeling

Landslide hazard mapping is the quantification of spatial and temporal probabilities of landslide occurrence. The spatial probability can be obtained using LSM. In the data-driven methods of LSM, landslide predisposing factors are evaluated simultaneously, which can be further applied to unaffected areas in similar conditions. The data-driven methods are mainly statistical and machine learning algorithms. Support vector machine (SVM) is based on the principle of the Vapnik–Chervonenkis dimension and structural risk minimization. The input variables are mapped to a high-dimension linear space by nonlinear transformation to construct the optimal decision function. The SVM model searches for an optimal surface in the feature space to separate positive (landslide) from the negative (non-landslide) types (Peng et al. 2014). SVM has been successfully used in landslide detection (e.g., Marjanović et al. 2011; Zhou et al. 2018a; Huang and Zhao 2018; Dou et al. 2020).

The landslide susceptibility map has been produced through an integrated algorithm of Information Gain and SVM (Yu et al. 2019). The variables considered for the LSM are extracted from the following available maps and data layers: the existing landslide inventory map (Fig. 1(c)), surface elevation, the geological maps, and the topographical map. According to the field survey and preliminary results in TGRA (Bai et al. 2010; Wu et al. 2013; Peng et al. 2014), fourteen predisposing factors are initially considered and prepared, namely altitude, slope, aspect, curvature, plan curvature, profile curvature, stream power index (SPI), topographic wetness index (TWI), terrain roughness index (TRI), lithology, bedding structure, distance to faults, distance to rivers, and distance to gullies. After multicollinearity analysis and importance calculation, the altitude, curvature, plan curvature, profile curvature, and TWI are removed (Yu et al. 2019). Finally, nine predisposing factors are selected as inputs for LSM (see Table 1 for details). In our study, the

variables have been resampled to the same 20-by-20-m pixels. We use 70% of the known landslides for training, and the remaining 30% are for validation. Radial basis function (RBF)-based SVM is used to construct the relationship between the spatial probability of landslide occurrence and its predisposing factors. Through the trial and error method, the parameters of penalty function and RBF are set as 20 and 1.3, respectively. The detailed information of LSM can be found in Yu et al. (2019).

#### Statistics of rainfall and landslides

In this study, the rainfall datasets are collected from a rain gauge which is about 2 km from the urban area of Wushan ( $109^{\circ}52'05''E$ ,  $31^{\circ}05'55''N$ ). The rain gauge has been collecting data once a day since 1960. A total of 158 landslides that occurred between 1995 and 2015 are selected as samples. July 1998 witnessed unprecedented rainfall with 5-day rainfall total exceeding 300 mm (Fig. 2). The severe rainfall induced the failure of 25 landslides, accounting for 15.8% of the landslide inventory. Thereafter, a total of 38 landslides failed in 2003 due to a combined effect of wet season and the first impoundment of the TGRA (Fig. 2). Liu (2014) has demonstrated that the antecedent 5-day rainfall total is mostly correlated with landslide events in TGRA. Therefore, we use it to represent rainfall when comparing with the landslide occurrence probability.

#### Landslide hazard mapping using probability analysis

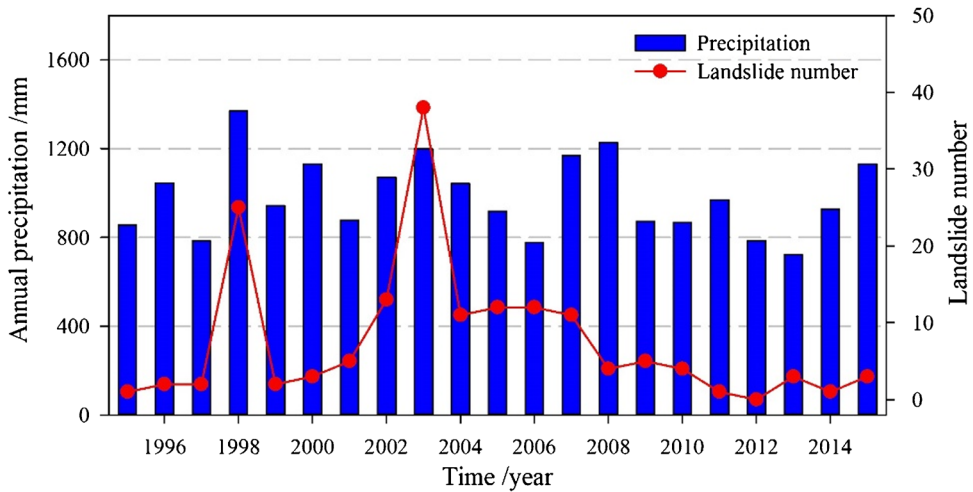
The temporal probability of landslide occurrence is generally expressed in terms of frequency/return period of recurring landslide events (Corominas et al. 2014). The frequency represents the number of events in a certain time interval or for a type of specific triggering event (e.g., earth shaking or rainfall) (Bordoni et al. 2020). Here, we consider the rainfall. The landslide hazard index  $H$  is given by

$$H = P(s) \times P(t) \times P(l) \quad (1)$$

**Table 1** Predisposing factors. Original data were collected by the Chongqing Bureau of Planning and Natural Resources

Predisposing factors	Notes
Slope angle	The steepness or the degree of incline of a surface.
Aspect	The orientation of the largest topographic gradient with respect to the north
SPI	A measure of the erosive power of flowing water given by $SPI = As \times \tan(\beta)$ , where $As$ is the specific contributing area and $\beta$ is the slope angle
TRI	The degree of surface erosion and the complexity of topographic relief, i.e., the ratio of surface area to projected area of surface unit. TRI is given by $TRI = 1/\cos(\beta)$ , where $\beta$ is the slope angle
Lithology	A description of its physical characteristics visible at outcrop, in hand or core samples. Physical characteristics include color, texture, grain size, and composition. It was extracted from the geological map
Bedding structure	The intersection relationship between strata and slope. More details can be found in Zhou et al. (2018a)
Distance to faults	Characterizes the first-order intensity of fractures in rock mass near the faults
Distance to rivers	Represents its exposure to the river erosion
Distance to gullies	Characterizes the influence strength of the gully on the landslide

**Fig. 2** Landslide number and annual rainfall total from 1995 to 2015



where  $P(s)$  is the spatial probability of landslide occurrence,  $P(t)$  is the temporal probability of a particular triggering event, and  $P(l)$  is the probability of the landslide failure in response to the triggering event. We assume that the specific triggering event is about to occur and  $P(t)$  equals 1. And thus, Eq. 1 can be simplified as  $P(s) \times P(l)$ .

### The principle of SBAS InSAR

SBAS InSAR method relies on a collection of interferograms with comparatively small temporal intervals and short perpendicular baselines. Phase  $\psi$  in an interferogram reflects the difference in the round-trip distance from sensors to monitoring targets,

$$\psi = W\{\phi_D + \phi_T + \phi_A + \phi_O + \phi_N\} \quad (2)$$

where  $\phi_D$ ,  $\phi_T$ ,  $\phi_A$ ,  $\phi_O$ , and  $\phi_N$  are the phase components due to ground deformation, topographic error, atmospheric disturbance, inaccurate orbit information, and other noise, respectively. The phase of ground deformation can be obtained by removing other phase components via spatial and temporal filters. Based on the singular value decomposition and minimum norm criterion of deformation rate, we can resolve time-series deformation products in forms of secular rates and cumulative displacement time series (Berardino et al. 2002; Hooper et al. 2004).

The Sentinel-1 SAR satellite mission launched by the European Space Agency in 2014 comprises a constellation of two near-polar orbiting satellites with C-band SAR sensors, which operates with a revisit time of 12 days from each individual satellite and 6 days from two consecutive satellites (Ma et al. 2021). Because the triggering factors of landslide in TGRA (rainfall and reservoir water level fluctuation) change periodically within 1 year, landslide hazard intensity in different water years is similar (Cao et al. 2016; Tang

et al. 2019). Differently from previous work (Segoni et al. 2014; Fu et al. 2020; Wang et al. 2020a, b), here we focus on the details of intra-annual variations to try to predict small changes by combining methods of probability analysis and MT-InSAR. Here we focus on 1 water year from September 30, 2016, to September 13, 2017, with a collection of 28 ascending Sentinel-1 images (Fig. 3).

The processing of radar images using MT-InSAR comprises of interferogram generation and time-series analysis. In this study, the threshold values of temporal and perpendicular baselines are 90 days and 1000 m, respectively. We use the 1 arc-second void-filled version of the Shuttle Radar Topography Mission digital elevation model to simulate the topographic phase and generate differential interferograms. Subsequently, the SBAS module in StaMPS is employed for the MT-InSAR analysis to derive the time-series displacements and velocities. We select monitoring targets with coherence above the threshold of 0.6 (Morishita et al. 2020; Zhou et al. 2020a, b). The slope orientation of the study area is mostly north-south, to which the InSAR technique is less sensitive. We use the LOS measurements rather than a down-slope projection of the LOS rates (Hilley et al. 2004; Hu et al. 2018).

### MT-InSAR-assisted dynamic hazard mapping

The time-series displacements obtained from MT-InSAR can be used as the supplement for an enhanced landslide hazard mapping initially achieved by the probability analysis (“[The principle of landslide hazard mapping](#)”). Our framework consists of five steps (Fig. 4): (i) predict the spatial probability of landslide occurrence using machine learning methods SVM; (ii) calculate the temporal probability of landslide occurrence in response to the triggering events; (iii) initialize a preliminary landslide hazard map using

**Fig. 3** The time distribution of Sentinel-1 imagery

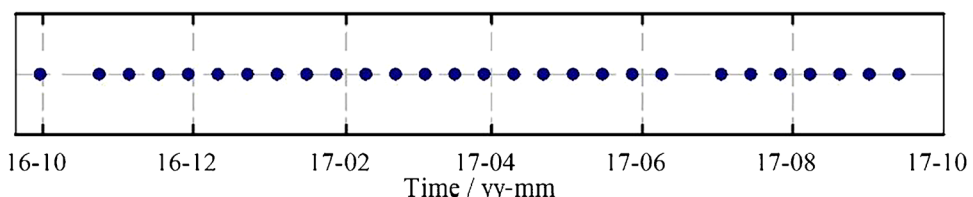
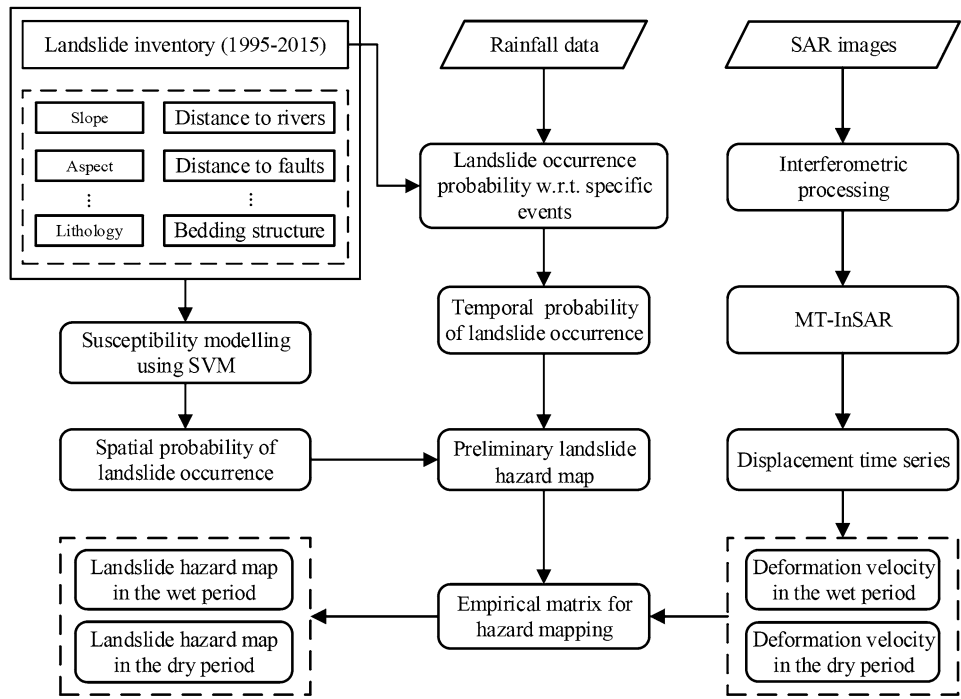


**Fig. 4** The flowchart of MT-InSAR-assisted landslide hazard mapping



spatial and temporal probabilities; (iv) extract the time-dependent ground deformation velocities using MT-InSAR method; (v) finalize a landslide hazard map by integrating ground deformation and the preliminary hazard map.

## Results

### Preliminary landslide hazard map

#### Landslide susceptibility map

The susceptibility map produced by SVM is shown in Fig. 5(a). The predicted spatial probability is within the range of 0 to 0.988. The statistics are shown in Table 2. The spatial probability value of 53.90% pixels is less than 0.1, and most of them are far away from

the Yangtze River. It means that the influence of the Yangtze River on landslide stability is only within a certain range of both banks. The spatial probability of 21.40% pixels is larger than 0.8. Most of them are distributed on two sides of the Yangtze River (Fig. 5(a)). The susceptibility map and statistics indicate that the distance to rivers is the main predisposing factor of landslide spatial development, which is also evident from the factor importance ranking (Yu et al. 2019).

The receiver operating characteristics (ROC) curve (Hanley and McNeil 1983) is used to assess the performance. The area under the ROC curve (AUC) can be considered an accuracy index, and the model with an AUC larger than 0.8 has an excellent performance (Mandrekar 2010). The AUCs in training and validation are 0.927 and 0.922, respectively (Fig. 5(b)). It helps in verifying the performance of our trained model and the consequent susceptibility map.

**Fig. 5** **a** The susceptibility map produced by SVM. **b** The ROCs of SVM

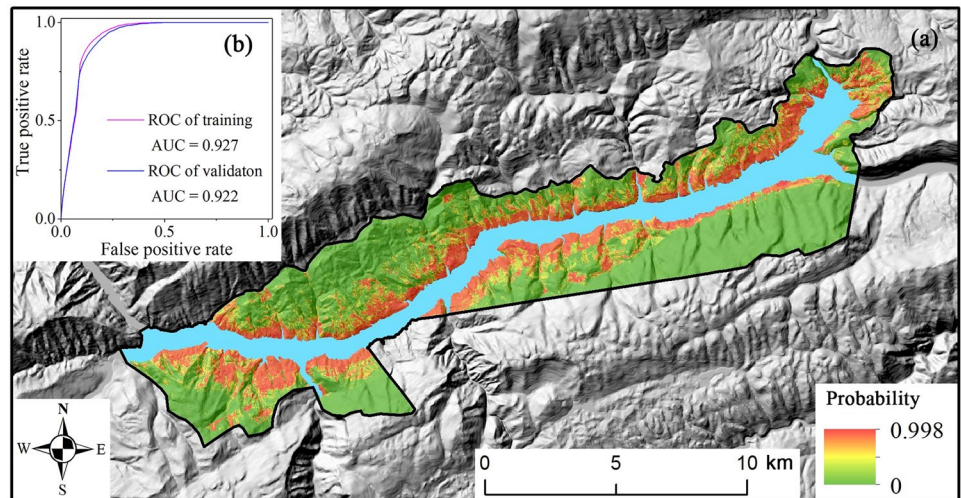


**Table 2** Statistics of susceptibility map

Probability	No. pixels	%
0.0–0.1	152,294	53.90
0.1–0.2	15,192	5.38
0.2–0.3	10,229	3.62
0.3–0.4	8,347	2.95
0.4–0.5	7,191	2.55
0.5–0.6	7,903	2.80
0.6–0.7	8,459	2.99
0.7–0.8	12,481	4.42
0.8–0.9	47,008	16.64
0.9–1.0	13,442	4.76

**Table 3** Statistics of rainfall events and landslide occurrence

	Antecedent 5-day rainfall total (mm)			
	0	0–50	50–100	>100
<b>Rainfall event</b>				
Number	1,082	5,838	429	91
Proportion	14.54%	78.47%	5.77%	1.22%
<b>Landslide occurrence</b>				
Number	0	36	75	47
Proportion	0	22.78%	47.47%	29.75%
Temporal probability of landslide occurrence	0	0.006	0.175	0.517

### Landslide hazard mapping

The antecedent 5-day rainfall total is classified into four groups: 0, 0–50, 50–100, and >100 mm (Liu et al. 2014). For two decades from 1995 to 2015 (Table 3), the rainfall condition of 0–50 mm occurred 5838 times, while the conditions of 50–100 mm and >100 mm occurred 429 and 91 times, respectively. When the antecedent 5-day rainfall total is greater than 100 mm, 47 landslides were triggered, accounting for 29.75% of the total landslide events in this period. A total of 36 and 75 landslide events occurred when the antecedent 5-day rainfall total is 0–50 mm and 50–100 mm, accounting for 22.78% and 47.47% of the landslide inventory, respectively. The temporal probabilities of landslide occurrence under the four rainfall conditions are 0, 0.006, 0.175, and 0.517, respectively.

Based on the predicted landslide spatial probability  $P(s)$  (Fig. 5) and the temporal probability of landslide occurrence under different rainfall conditions  $P(l)$  (Table 3), we obtain the landslide hazard index  $H$  referring to Eq. 1 (Fig. 6).

### Ground deformation

The ground deformation velocity obtained from MT-InSAR is shown in Fig. 7. A total of 233,848 monitoring points are captured in our study area, resulting in a density of 1665 point/km<sup>2</sup>. The standard deviation of LOS velocity is 7.6, and we set two times the standard deviation as the stability threshold (Barra et al. 2017; Solari et al. 2020). The deformation velocities of 72.94% monitoring points are between –15 and 15 mm/year. This seems to show that most slopes of the study area are stable. The largest velocities in LOS directions are 85.65 mm/year and –96.17 mm/year, respectively.

We focus on the Shuizhuyuan landslide near Yangtze River to interpret the temporal characteristics of deformation and inducing factors of rainfall and reservoir level fluctuation (Figs. 7 and 8). The deformation velocity of Shuizhuyuan landslide presents significant difference in dry and wet seasons. During the dry season from October 2016 to March 2017, it was in a stable condition due to the high reservoir water level and scarce rainfall at TGRA, and the deformation velocity is 0.14 mm/month. During the wet season from April to September 2017, influenced by the rapid drawdown of reservoir water level and abundant rainfall, the deformation accelerated to –13.04 mm/month.

### Landslide hazard mapping assisted by deformation rates

Many bank landslides in TGRA move slowly. They creep at rates ranging from millimeters to several meters per year and can persist for years to decades (Yin et al. 2010; Zhou et al. 2016; Tang et al. 2019; Juang 2021). The reservoir water level in TGRA is similar throughout different years. It fluctuates between 145 and 175 m every year (Fig. 8), controlled by the hydraulic engineering operation at the Three Gorges Dam. In response to the seasonal rainwater recharge and reservoir water loading and seepage, landslides present greater rates during the wet season from April to September when a dynamic failure is more likely to occur. In the dry season, landslide motions are more idle with smaller potential to fail due to less rainfall and gradual change of the reservoir water level. So the probability of landslide occurrence is time varying. We focus on one complete water year during 2016–2017 and divide it into two for their respective hazard mapping. We rely on MT-InSAR method to compute the deformation velocities during the dry season of 9/30/2016 to 3/29/2017 and the wet season of 3/29/2017–9/13/2017. We use the Ordinary Kriging method to interpolate the displacement fields in space (Fig. 9). It is conducted in ArcGIS 10.2 and the cell size is set as 20 m as well.

Based on field investigation, we divide the obtained landslide hazard index into four tiers: H1 (0–0.0021), H2 (0.0021–0.0700), H3 (0.0700–0.1607), and H4 (>0.1607). Meanwhile, the monthly surface deformation velocities are also categorized into four levels: V1 (0–2 mm/month), V2 (2–4 mm/month), V3 (4–6 mm/month), and V4 (>6 mm/month). With the combination of the preliminary hazard levels and deformation velocities, an assessment matrix is proposed for landslide hazard mapping (Table 4). The hazard mapping results of the two periods are shown in Figs. 10 and 11.

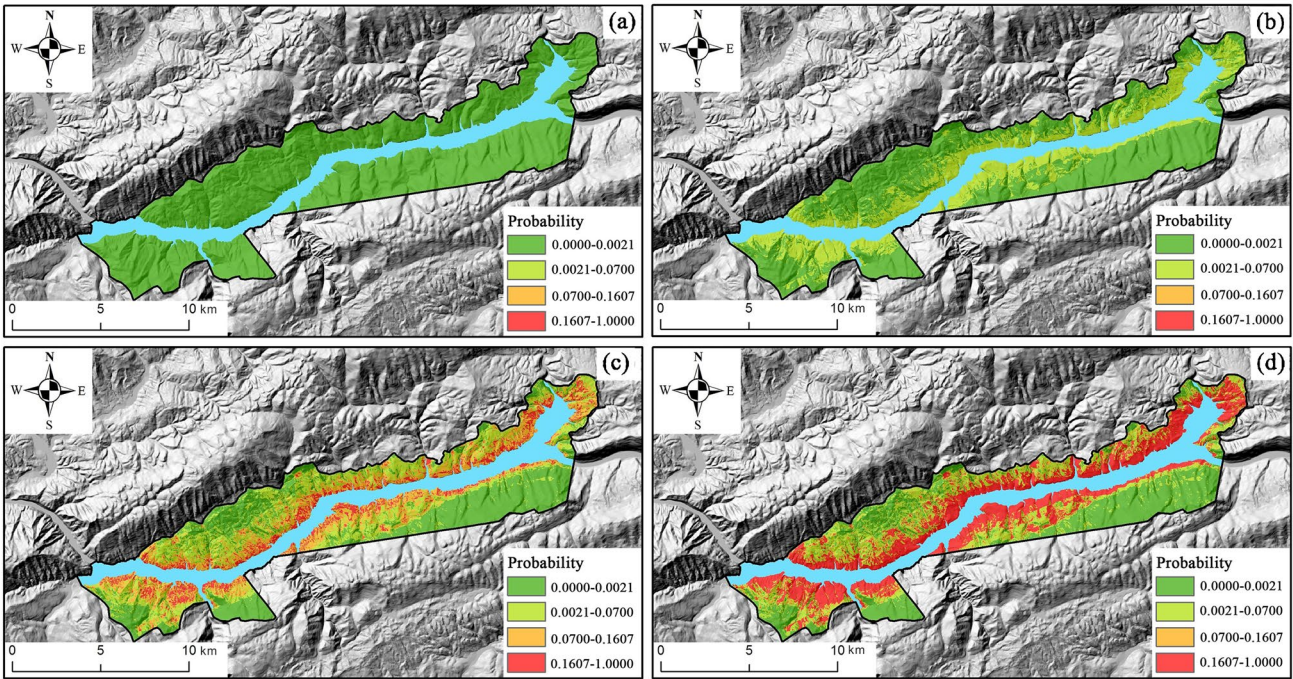
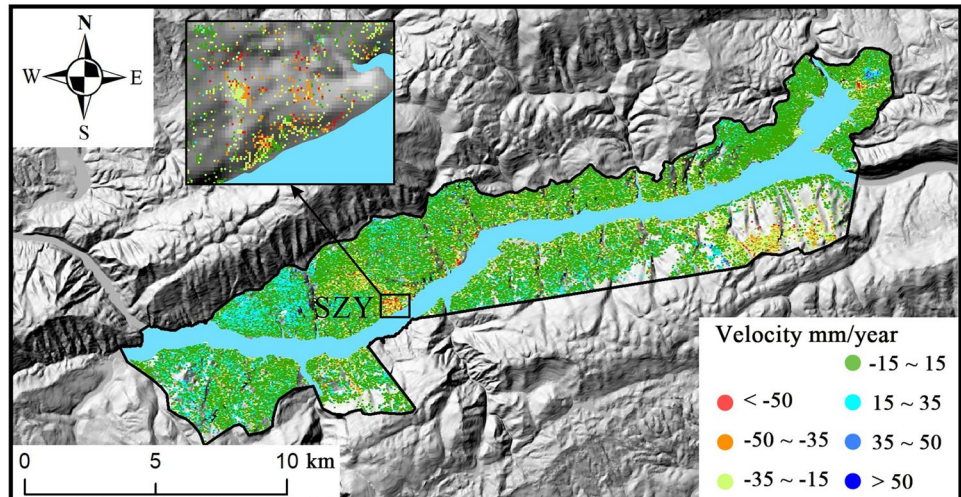


**Fig. 6** The preliminary landslide hazard maps when the antecedent 5-day rainfall total is **a** 0, **b** 0–50, **c** 50–100, and **d** > 100 mm, respectively

**Fig. 7** The LOS deformation velocity from 9/30/2016 to 9/13/2017. SZY refers to Shuizhuyuan landslide



## Discussion

### Landslide hazard under different rainfall conditions

In the dry season of 9/30/2016–3/29/2017, TGRA was under the condition of high reservoir water level and scarce rainfall. More than 97% of the study area was in the hazard levels of Low/Very Low. In the wet season of 3/29/2017–9/13/2017, the rapid fluctuation of reservoir water levels and intense rainfall destabilized the landslides. MT-InSAR results show that the landslide accelerated during this period, such as at the Shuizhuyuan landslide and Taping landslide (Fig. 9). When the antecedent 5-day rainfall

reaches 50–100 and > 100 mm, the proportions of pixels showing High and Moderate hazard levels increase to 10.41% and 22.56%, respectively (Table 5).

The intensity of rainfall is correlated with the landslide hazard. Our statistics demonstrate that the area with the Very Low hazard level reduced when the rainfall increases, and vice versa. When the antecedent 5-day rainfall total exceeds 100 mm, the proportion of pixels with High hazard level peaks at 0.06% and 2.27%, while the Very Low hazard level is the least at 55.21% and 41.84%, respectively. Meanwhile, when the antecedent 5-day rainfall total is less than 50 mm, 0.02% and 0.38% of areas are in High hazard level in dry and wet season, respectively (Table 5).

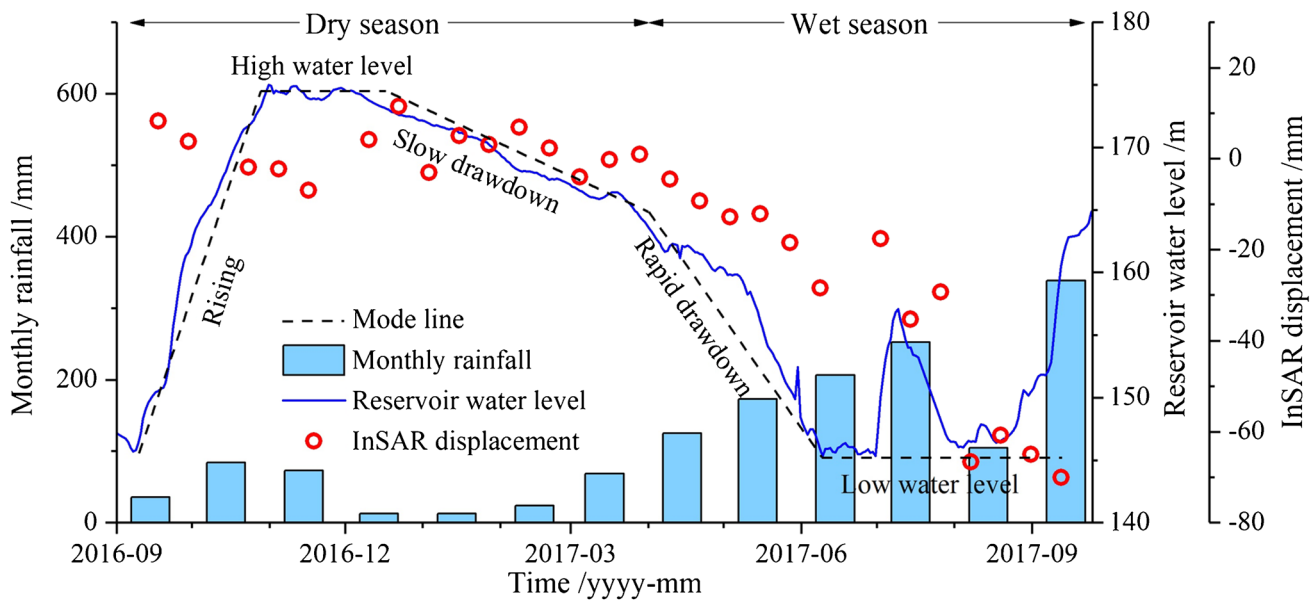


**Fig. 8** InSAR displacement time-series of Shuizhuyuan landslide, reservoir level, and rainfall over the TGRA from 2016 to 2017

**Fig. 9** The InSAR line-of-sight (LOS) displacement velocity during **a** the dry season from 9/30/2016 to 3/29/2017) and **b** the wet season from 3/29/2017 to 9/13/2017

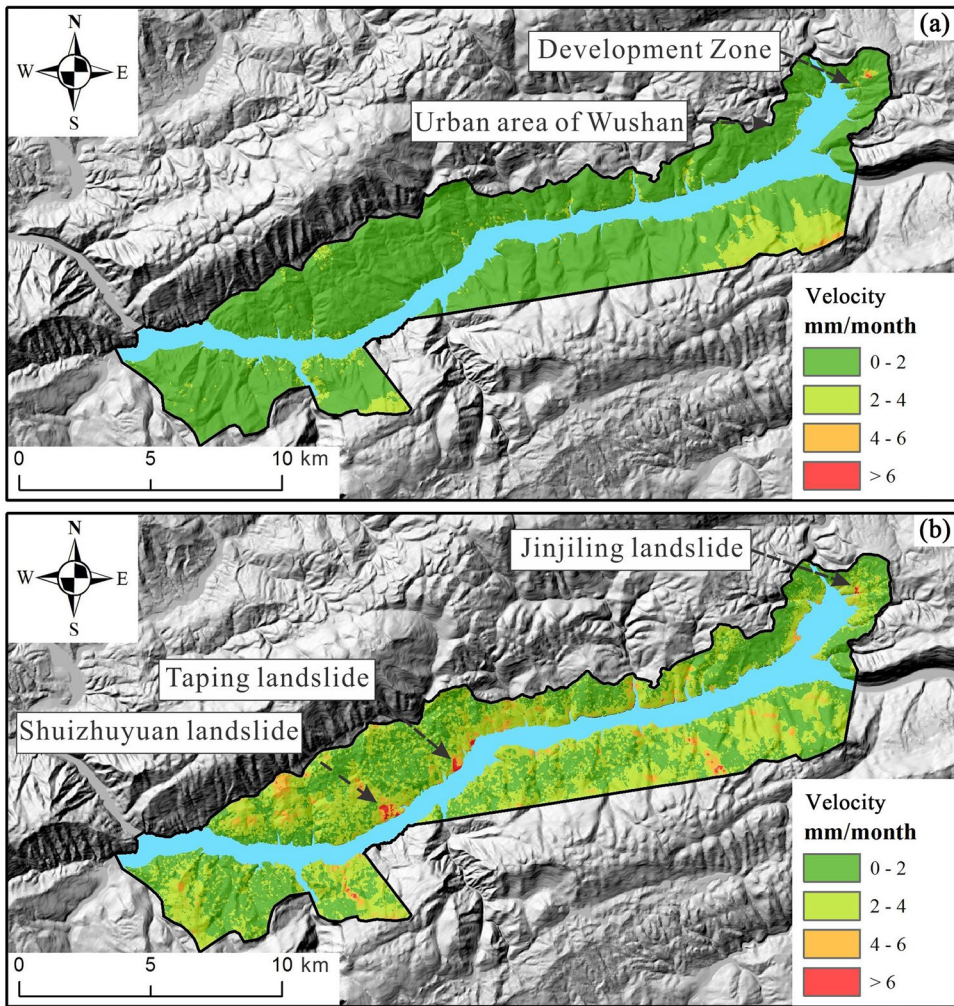


**Table 4** The matrix of landslide hazard mapping integrating the preliminary landslide hazard tiers (H1–4) and ground deformation velocities (V1–4)

	V4	V3	V2	V1
H4	4	4	3	2
H3	4	3	2	2
H2	4	3	2	1
H1	4	3	1	1

#### Accuracy improvement from MT-InSAR displacement measurements

##### False-positive error

With the slope stabilization using engineering treatment or dormancy of landslides, landslide hazard level can be reduced. It will cause false-positive error in hazard maps without previous identification of landslide hazard. For example, in Wushan urban area, many detected landslide terrains have been confirmed false high-hazard-level by field investigation. As the result of the slope treatment, the Wushan urban area did not deform during the period between 2016 and 2017, which is supported by field investigation and MT-InSAR results (Fig. 9). The MT-InSAR-assisted method effectively reduces the false-positive error (Figs. 10 and 11). In

our proposed method, when the antecedent 5-day rainfall total is 50–100 mm, the proportions of pixels in Moderate and High hazard levels are reduced by 24.34% (34.76–10.41%) and 33.52% (34.76–1.24%) in wet and dry seasons, respectively (Tables 5 and 6).

##### False-negative error

The false-negative error may lead to fatal decisions in urban planning. The main reason for the false-negative error is unrecognized landslides or outdated landslide inventory. Anthropogenic modification (e.g., loading, excavation) on the slopes to meet with the engineering demands may break up the force equilibrium of natural slopes, such as the Jinjiling landslide. The freely available Sentinel-1 satellite imagery and the widely used MT-InSAR data processing methods provide a cost- and time-efficient tool to measure the ground deformation. The continuous deformation information can be effectively incorporated to update the hazard maps and to reduce the false-negative errors. For example, when the rainfall is less than 50 mm, no region is exposed to High/Moderate landslide hazard level. With the help of the deformation measurements, the hazard map of the mobile Jinjiling landslide can be updated (Fig. 10(a) and (b)). The proportions of pixels in High and Moderate hazard levels increase by 0.43% (0–0.43%) and 4.93% (0–4.93%) in dry and wet seasons, respectively (Tables 5 and 6).

#### Dynamic landslide hazard assessment

The landslide hazard is dynamic in response to the environmental variabilities. Here we consider two representative time frames

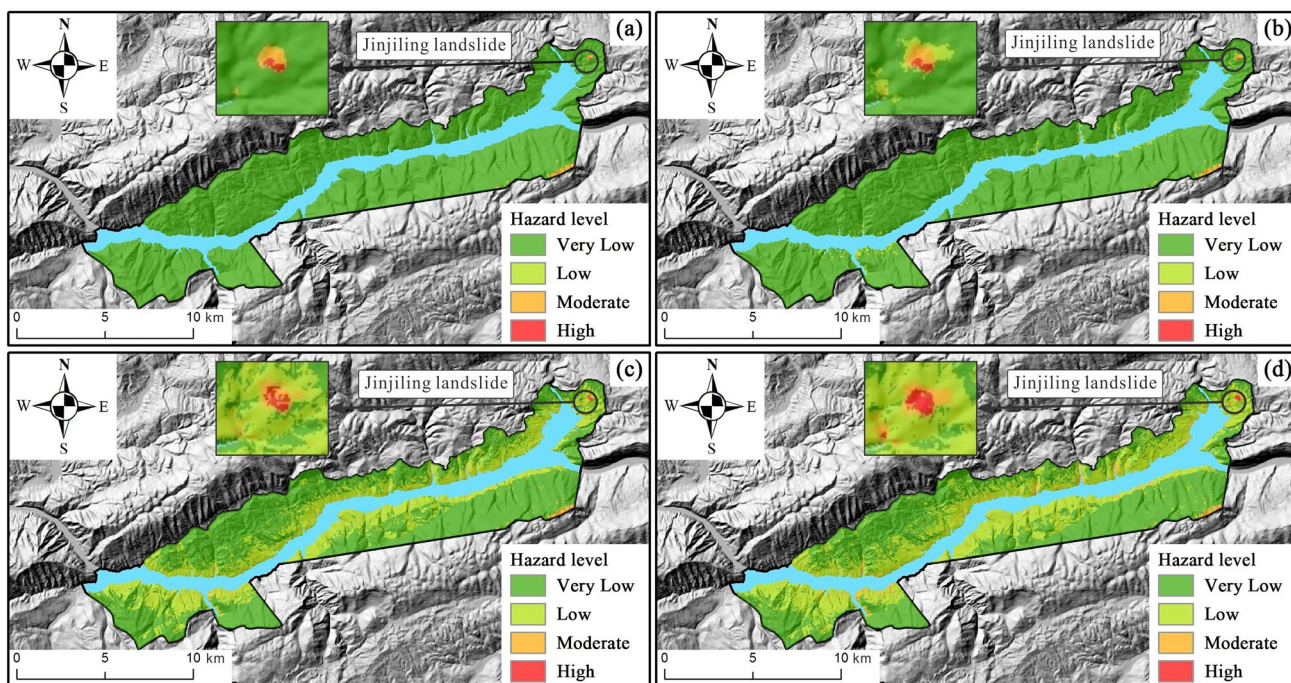


**Fig. 10** The landslide hazard maps during 9/30/2016–3/29/2017 when the antecedent 5-day rainfall total is **a** 0, **b** 0–50, **c** 50–100, and **d**>100 mm. Black circles show the location of the Jinjiling landslide

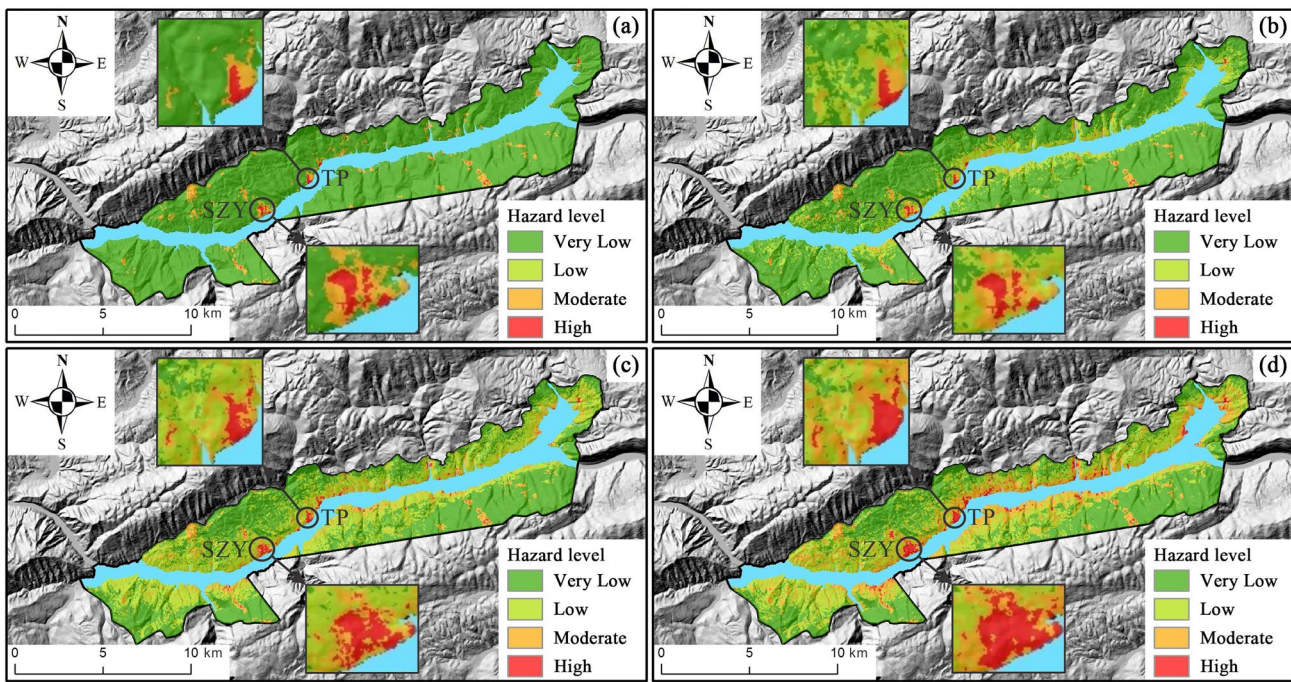


**Fig. 11** The landslide hazard maps during 3/19/2017–9/13/2017 when the antecedent 5-day rainfall total is **a** 0, **b** 0–50, **c** 50–100, and **d** >100 mm. TP refers to Taping landslide and SZY refers to Shuizhuyuan landslide. Black circles show the locations of the Taping and Shuizhuyuan landslides

**Table 5** Statistics on the landslide hazard

Pixels exposed to the landslide hazard	Antecedent 5-day rainfall total (mm)							
	0		0–50		50–100		>100	
	No	%	No	%	No	%	No	%
<b>Dry season: 9/30/2016–3/29/2017</b>								
High	47	0.02	47	0.02	106	0.04	175	0.06
Moderate	1,159	0.41	1,159	0.41	3,376	1.20	6,866	2.43
Low	0	0.00	5,784	2.05	97,444	34.55	119,294	42.30
Very low	280,830	99.57	275,046	97.52	181,110	64.22	155,701	55.21
<b>Wet season: 3/29/2017–9/13/2017</b>								
High	1082	0.38	1,082	0.38	3,185	1.13	6,416	2.27
Moderate	12,829	4.55	12,829	4.55	26,159	9.28	57,198	20.28
Low	0	0.00	48,654	17.25	113,783	40.34	100,414	35.60
Very low	268,125	95.07	219,471	77.82	138,909	49.25	118,008	41.84

of dry and wet seasons for landslide hazard mapping. In the dry season of 9/30/2016–3/29/2017, the proportions of pixels in High hazard level under four rainfall conditions are 0.02%, 0.02%, 0.04%, and 0.06%, respectively (Table 5). Only the Jinjiling landslide was deforming (6.52 mm/month) and at a High hazard level. The excavation of the road in front of the landslide formed a high steep free face, providing the necessary conditions for slip and shearing. That

is the reason why the Jinjiling landslide experienced large deformation with small rainfall amounts (Yan et al. 2019). In the wet season of 3/29/2017–9/13/2017, the number of the deformed pixel (>4 mm/month) increases by 12,705. In addition to the accelerated deformation of the Jinjiling landslide induced by rainfall, the deformation of many reservoir landslides also accelerated under a combined impact of heavy rainfall and rapid fluctuation of reservoir water

**Table 6** Statistics of the preliminary hazard maps

Pixels exposed to the landslide hazard	Antecedent 5-day rainfall total (mm)							
	0		0–50		50–100		>100	
	No	%	No	%	No	%	No	%
High	0	0.00	0	0.00	31,530	11.16	103,795	36.74
Moderate	0	0.00	0	0.00	66,679	23.60	19,860	7.03
Low	0	0.00	101,492	35.92	83,803	29.66	74,306	26.30
Very Low	282,546	100.00	181,054	64.08	100,534	35.58	84,585	29.94

levels, such as in the Taping landslide and Shuizhuyuan landslide (Fig. 9). In June 2017, a tension crack developed in the Taping landslide, with a strike of approximately 33°, length of 20 m, width of approximately 10 cm, and visible depth of 1 m (Zhang et al. 2021). During this period, the proportions of pixels in the High hazard level under four rainfall conditions are 0.38%, 0.38%, 1.13%, and 2.27%, respectively (Table 5). The MT-InSAR-assisted results show that the landslide hazard varies in different seasons and rainfall conditions (Figs. 10 and 11). The multi-temporal hazard maps can be better inform the actual landslide occurrence. Compared with the statistical hazard maps (Fig. 6), multi-temporal hazard maps can help in rapidly locating hazard sources changing over time, which can guide hazard detection more accurately and improve the efficiency of risk control. In the dry season, more attentions should be paid to the Jinjiling landslide because it is one of the few landslides still in active motion. In the wet season, rainwater and rapid drawdown of reservoir water level may reactivate the reservoir landslides and promote the landslide acceleration; more attentions should be paid on these landslides.

### The feasibility of MT-InSAR-assisted method

The deformation velocity extracted by the MT-InSAR technique is a crucial input in our proposed method, and it is a premise for the accurate hazard mapping. MT-InSAR approach is feasible to map slow motions rather than fast motions due to the intrinsic theory of interferometry, the configuration of the radar wavelength, and the revisiting time of the platform (Wasowski and Bovenga 2014; Ciampalini et al. 2016). The mapping method produces more reliable results in regions with no or sparse vegetated covers, so that the temporal and volumetric decorrelation is reduced. The shadow phenomenon often exists in SAR image in mountainous terrains (Novellino et al. 2017). The MT-InSAR method with multi-platform and multi-track SAR images is suggested to reduce the shadow effect. In addition, longer wavelength data (e.g., L-band) can better penetrate the vegetative canopies and maintain the coherence, and thus is recommended for the MT-InSAR-assisted hazard mapping for slow-moving landslides. However, the catastrophic evolution of landslide deformation patterns often starts from a transitional creep behavior that can be fruitfully observed by MT-InSAR and exploited, in case of progressive-like failures, to predict the time of failure by using inverse-velocity methods (Catani and Segoni 2021).

### Conclusion

In this paper, we implement the dynamic landslide hazard mapping by combining the spatiotemporal probability analysis and time-varying ground deformation velocities derived by MT-InSAR method. We consider two representative time frames of the dry and the wet seasons in 1 water year of 2016–2017. We specialize the 5-day rainfall totals in groups of 0, 0–50, 50–100, and >100 mm to conduct landslide hazard mapping using our proposed framework. Our results demonstrate that the landslide hazard levels elevate with increasing rainfall. InSAR ground deformation measurements are the key for dynamic landslide hazard mapping. They allow us to precisely outline the Shuizhuyuan landslide and Taping landslide. Landslide hazard mapping requires the best elimination of the false-positive/-negative error. The comparison with the preliminary hazard maps and field survey suggests that the false errors can be effectively corrected after compiling the ground deformation velocities. The integration of time-varying ground velocities allows for a more accurate mapping of the dynamic landslide hazards.

### Acknowledgements

The first author thanks Prof. Andy Hooper in Leeds University for his help in MT-InSAR processing. We thank the assistance of Chongqing Bureau of Planning and Natural Resources and Dr. Xin Liang for data collection. We appreciate the reviewers for their suggestions that significantly improved the quality of this paper.

### Funding

This research is funded by the National Natural Science Foundation of China (No. 41907253 and No. 41702330) and Key Research and Development Program of Hubei Province (No. 2021BCA219).

### Declarations

**Conflict of interest** The authors declare no competing interests.

### References

Ahmed B (2021) The root causes of landslide vulnerability in Bangladesh. *Landslides* 18(5):1707–1720

- Bai S, Wang J, Lü G, Zhou P, Hou S, Xu S (2010) GIS-based logistic regression for landslide susceptibility mapping of the Zhongxian segment in the Three Gorges area. *China Geomorphology* 115(1–2):23–31
- Barra A, Solari L, Béjar-Pizarro M, Monserrat O, Bianchini S, Herrera G, Crosetto M, Sarro R, González-Alonso E, Mateos R, Liguerzana S (2017) A methodology to detect and update active deformation areas based on Sentinel-1 SAR images. *Remote Sensing* 9:1002
- Bekaert DP, Handwerger AL, Agram P, Kirschbaum DB (2020) InSAR-based detection method for mapping and monitoring slow-moving landslides in remote regions with steep and mountainous terrain: an application to Nepal. *Remote Sens Environ* 249:111983
- Berardino P, Fornaro G, Lanari R, Sansosti E (2002) A new algorithm for surface deformation monitoring based on small baseline differential SAR interferograms. *IEEE Trans Geosci Remote Sens* 40(11):2375–2383
- Bontemps N, Lacroix P, Larose E, Jara J, Taipe E (2020) Rain and small earthquakes maintain a slow-moving landslide in a persistent critical state. *Nat Commun* 11(1):1–10
- Bordoni M, Vivaldi V, Lucchelli L, Ciabatta L, Brocca, L, Galve JP, Meisina C (2020) Development of a data-driven model for spatial and temporal shallow landslide probability of occurrence at catchment scale. *Landslides*, 1–21
- Bui DT, Pradhan B, Lofman O, Revhaug I (2012) Landslide susceptibility assessment in Vietnam using support vector machines, decision tree, and Naïve Bayes Models. *Mathematical problems in Engineering*, 2012
- Cao Y, Yin K, Alexander DE, Zhou C (2016) Using an extreme learning machine to predict the displacement of step-like landslides in relation to controlling factors. *Landslides* 13(4):725–736
- Cao Y, Yin K, Zhou C, Ahmed B (2020) Establishment of landslide groundwater level prediction model based on GA-SVM and influencing factor analysis. *Sensors* 20(3):845
- Catani F, Lagomarsino D, Segoni S, Tofani V (2013) Landslide susceptibility estimation by random forests technique: sensitivity and scaling issues. *Nat Hazard* 13(11):2815–2831
- Catani F, Segoni S (2021) Prediction and forecasting of mass-movements, Reference Module in Earth Systems and Environmental Sciences, Elsevier, 2021, ISBN 9780124095489, <https://doi.org/10.1016/B978-0-12-818234-5.00099-7>
- Chen T, Zhu L, Niu RQ, Trinder CJ, Peng L, Lei T (2020) Mapping landslide susceptibility at the Three Gorges Reservoir, China, using gradient boosting decision tree, random forest and information value models. *J Mt Sci* 17(3):670–685
- Chen W, Chen X, Peng J, Panahi M, Lee S (2021) Landslide susceptibility modeling based on ANFIS with teaching-learning-based optimization and Satin bowerbird optimizer. *Geosci Front* 12(1):93–107
- Ciampalini A, Raspini F, Lagomarsino D, Catani F, Casagli N (2016) Landslide susceptibility map refinement using PSInSAR data. *Remote Sens Environ* 184:302–315
- Corominas J, van Westen C, Frattini P, Cascini L, Malet JP, Fotopoulou S, Catani F, Van Den Eeckhaut M, Mavrouli O, Agliardi F, Pitilakis K, Winter MG, Pastor M, Ferlisi S, Tofani V, Hervás J, Smith JT (2014) Recommendations for the quantitative analysis of landslide risk. *Bull Eng Geol Env* 73(2):209–263
- Dai K, Li Z, Xu Q, Burgmann R, Milledge DG, Tomas R, Fan X, Zhao C, Liu X, Peng J, Zhang Q, Wang Z, Qu T, He C, Li D, Liu J (2020) Entering the era of earth observation-based landslide warning systems: a novel and exciting framework. *IEEE Geosci Remote Sens Mag* 8(1):136–153
- Dong J, Liao M, Xu Q, Zhang L, Tang M, Gong J (2018) Detection and displacement characterization of landslides using multi-temporal satellite SAR interferometry: a case study of Danba County in the Dadu River Basin. *Eng Geol* 240:95–109
- Dou J, Yunus AP, Bui DT, Merghadi A, Sahana M, Zhu Z, Chen CW, Han Z, Pham BT (2020) Improved landslide assessment using support vector machine with bagging, boosting, and stacking ensemble machine learning framework in a mountainous watershed. *Japan Landslides* 17(3):641–658
- Ferretti A, Fumagalli A, Novali F, Prati C, Rocca F, Rucci A (2011) A new algorithm for processing interferometric data-stacks: SqueeSAR. *IEEE Trans Geosci Remote Sens* 49(9):3460–3470
- Ferretti A, Prati C, Rocca F (2001) Permanent scatterers in SAR interferometry. *IEEE Trans Geosci Remote Sens* 39(1):8–20
- Froude MJ, Petley DN (2018) Global fatal landslide occurrence from 2004 to 2016. *Nat Hazard* 18(8):2161–2181
- Fu S, Chen L, Woldai T, Yin K, Gui L, Li D, Du J, Zhou C, Xu Y, Lian Z (2020) Landslide hazard probability and risk assessment at the community level: a case of western Hubei, China. *Nat Hazard* 20(2):581–601
- Guzzetti F, Reichenbach P, Ardizzone F, Cardinali M, Galli M (2006) Estimating the quality of landslide susceptibility models. *Geomorphology* 81(1–2):166–184
- Guzzetti F, Reichenbach P, Cardinali M, Galli M, Ardizzone F (2005) Probabilistic landslide hazard assessment at the basin scale. *Geomorphology* 72(1–4):272–299
- Gomez H, Kavzoglu T (2005) Assessment of shallow landslide susceptibility using artificial neural networks in Jabonosa River Basin Venezuela. *Eng Geol* 78(1–2):11–27
- Hanley JA, McNeil BJ (1983) A method of comparing the areas under receiver operating characteristic curves derived from the same cases. *Radiology* 148(3):839–843
- Handwerger AL, Booth AM, Huang M-H, Fielding EJ (2021) Inferring the subsurface geometry and strength of slow-moving landslides using 3-D velocity measurements from the NASA/JPL UAVSAR. *J Geophys Res Earth Surf* 126:e2020JF005898. <https://doi.org/10.1029/2020JF005898>
- Hilley GE, Bürgmann R, Ferretti A, Novali F, Rocca F (2004) Dynamics of slow-moving landslides from permanent scatterer analysis. *Science* 304(5679):1952–1955
- Hong H, Liu J, Zhu AX (2020) Modeling landslide susceptibility using LogitBoost alternating decision trees and forest by penalizing attributes with the bagging ensemble. *Sci Total Environ* 718:137231
- Hong H, Miao Y, Liu J, Zhu AX (2019) Exploring the effects of the design and quantity of absence data on the performance of random forest-based landslide susceptibility mapping. *CATENA* 176:45–64
- Hooper A, Zebker H, Segall P, Kampes B (2004) A new method for measuring deformation on volcanoes and other natural terrains using InSAR persistent scatterers. *Geophys Res Lett*, 31 (23)
- Hu X, Bürgmann R, Fielding EJ, Lee H (2020) Internal kinematics of the Slumgullion landslide (USA) from high-resolution UAVSAR InSAR data. *Remote Sens Environ* 251:112057
- Hu X, Lu Z, Pierson TC, Kramer R, George DL (2018) Combining InSAR and GPS to determine transient movement and thickness of a seasonally active low-gradient translational landslide. *Geophys Res Lett* 45(3):1453–1462
- Huang J, Asch T, Wang C, Li Q (2019) Study on the combined threshold for gully-type debris flow early warning. *Nat Hazard* 19(1):41–51
- Huang Y, Zhao L (2018) Review on landslide susceptibility mapping using support vector machines. *CATENA* 165:520–529
- Intrieri E, Carlà T, Farina P, Bardi F, Ketizmen H, Casagli N (2019) Satellite interferometry as a tool for early warning and aiding decision making in an open-pit mine. *IEEE J Sel Top Appl Earth Obs Remote Sens* 12(12):5248–5258
- Juang CH (2021) BFTS-Engineering geologists' field station to study reservoir landslides. *Eng Geol* 284:106038
- Kawagoe S, Kazama S, Sarukkalige PR (2010) Probabilistic modelling of rainfall induced landslide hazard assessment. *Hydrol Earth Syst Sci* 14(6):1047–1061
- Lacroix P, Handwerger AL, Bièvre G (2020) Life and death of slow-moving landslides. *Nat Rev Earth Environ* 1(8):404–419
- Lee S, Sambath T (2006) Landslide susceptibility mapping in the Damrei Romel area, Cambodia using frequency ratio and logistic regression models. *Environ Geol* 50(6):847–855
- Liu C (2014) Landslide risk assessment at Wanzhou urban area in the Three Gorges Reservoir. China University of Geosciences Press, Wuhan
- Liu X, Zhao C, Zhang Q, Lu Z, Li Z, Yang C, Zhu W, Zeng J, Chen L, Liu C (2021) Integration of Sentinel-1 and ALOS/PALSAR-2 SAR datasets for mapping active landslides along the Jinsha River corridor, China. *Eng Geol*, 106033

- Lu P, Catani F, Tofani V, Casagli N (2014) Quantitative hazard and risk assessment for slow-moving landslides from Persistent Scatterer Interferometry. *Landslides* 11(4):685–696
- Ma P, Cui Y, Wang W, Lin H, Zhang Y (2021) Coupling InSAR and numerical modeling for characterizing landslide movements under complex loads in urbanized hillslopes. *Landslides*, 1–13
- Mandrekar JN (2010) Receiver operating characteristic curve in diagnostic test assessment. *J Thorac Oncol* 5(9):1315–1316
- Marjanović M, Kovačević M, Bajat B, Voženilek V (2011) Landslide susceptibility assessment using SVM machine learning algorithm. *Eng Geol* 123(3):225–234
- Morishita Y, Lazecky M, Wright T J et al (2020) LiCSBAS: an open-source InSAR time series analysis package integrated with the LiCSAR automated Sentinel-1 InSAR processor[J]. *Remote Sens* 12(3):424
- Neuhäuser B, Terhorst B (2007) Landslide susceptibility assessment using “weights-of-evidence” applied to a study area at the Jurassic escarpment (SW-Germany). *Geomorphology* 86(1–2):12–24
- Novellino A, Cigna F, Brahmi M, Sowter A, Bateson L, Marsh S (2017) Assessing the feasibility of a national InSAR ground deformation map of Great Britain with Sentinel-1. *Geosciences* 7(2):19
- Peng L, Niu R, Huang B, Wu X, Zhao Y, Ye R (2014) Landslide susceptibility mapping based on rough set theory and support vector machines: a case of the Three Gorges area, China. *Geomorphology* 204:287–301
- Pham BT, Phong TV, Nguyen-Thoi T, Parial K, KS Singh, Ly HB, Nguyen KT, Ho LS, Le HV, Prakash I (2020) Ensemble modeling of landslide susceptibility using random subspace learner and different decision tree classifiers. *Geocarto International*, 1–23
- Pourghasemi HR, Jirandeh AG, Pradhan B, Xu C, Gokceoglu C (2013) Landslide susceptibility mapping using support vector machine and GIS at the Golestan Province Iran. *J Earth Syst Sci* 122(2):349–369
- Pradhan B, Lee S (2010) Landslide susceptibility assessment and factor effect analysis: backpropagation artificial neural networks and their comparison with frequency ratio and bivariate logistic regression modelling. *Environ Model Softw* 25(6):747–759
- Solari L, Bianchini S, Franceschini R, Barra A, Monserrat O, Thuegaz P, Bertolo D, Crosetto M, Catani F (2020) Satellite interferometric data for landslide intensity evaluation in mountainous regions. *Int J Appl Earth Obs Geoinf* 87:102028
- Segoni S, Tofani V, Rosi A, Catani F, Casagli N (2018) Combination of rainfall thresholds and susceptibility maps for dynamic landslide hazard assessment at regional scale. *Front Earth Sci* 6:85
- Segoni S, Rosi A, Rossi G, Catani F, Casagli N (2014) Analysing the relationship between rainfalls and landslides to define a mosaic of triggering thresholds for regional-scale warning systems. *Nat Hazard* 14(9):2637–2648
- Tang H, Wasowski J, Juang CH (2019) Geohazards in the three Gorges Reservoir Area, China—lessons learned from decades of research. *Eng Geol* 261:105267
- Van Westen CJ, Rengers N, Soeters R (2003) Use of geomorphological information in indirect landslide susceptibility assessment. *Nat Hazards* 30(3):399–419
- Wang Z, Wang D, Guo Q, Wang D (2020a) Regional landslide hazard assessment through integrating susceptibility index and rainfall process. *Nat Hazards* 104(3):2153–2173
- Wang Y, Sun D, Wen H, Zhang H, Zhang F (2020b) Comparison of random forest model and frequency ratio model for landslide susceptibility mapping (LSM) in Yunyang County (Chongqing, China). *Int J Environ Res Public Health* 17(12):4206
- Wasowski J, Bovenga F (2014) Investigating landslides and unstable slopes with satellite multi temporal interferometry: current issues and future perspectives. *Eng Geol* 174:103–138
- Wasowski J, Pisano L (2020) Long-term InSAR, borehole inclinometer, and rainfall records provide insight into the mechanism and activity patterns of an extremely slow urbanized landslide. *Landslides* 17(2):445–457
- Wu X, Niu R, Ren F, Peng L (2013) Landslide susceptibility mapping using rough sets and back-propagation neural networks in the Three Gorges, China. *Environ Earth Sci* 70:1307–1318
- Xie M, Zhao W, Ju N, He C, Huang H, Cui Q (2020) Landslide evolution assessment based on InSAR and real-time monitoring of a large reactivated landslide, Wenchuan China. *Eng Geol* 277:105781
- Yan G, Yin Y, Huang B, Zhang Z, Zhu S (2019) Formation mechanism and characteristics of the Jinjiling landslide in Wushan in the Three Gorges Reservoir region China. *Landslides* 16(11):2087–2101
- Yin Y, Wang H, Gao Y, Li X (2010) Real-time monitoring and early warning of landslides at relocated Wushan Town, the Three Gorges Reservoir China. *Landslides* 7(3):339–349
- Yu L, Cao Y, Zhou C, Wang Y, Huo Z (2019) Landslide susceptibility mapping combining information gain ratio and support vector machines: a case study from Wushan segment in the Three Gorges Reservoir area China. *Appl Sci* 9(2):4756
- Zhang C, Yin Y, Yan H, Li H, Dai Z, Zhang N (2021) Reactivation characteristics and hydrological inducing factors of a massive ancient landslide in the three Gorges Reservoir China. *Eng Geol* 292:106273
- Zhang Y, Meng X, Dijkstra TA, Jordan CJ, Chen G, Zeng R, Novellino A (2020) Forecasting the magnitude of potential landslides based on InSAR techniques. *Remote Sens Environ* 241:111738
- Zhou C, Yin K, Cao Y, Li Y (2020a) Landslide susceptibility assessment by applying the coupling method of radial basis neural network and Adaboost: A case study from the Three Gorges Reservoir Area. *Earth Sci* 45(6):1865–1876
- Zhou C, Cao Y, Yin K, Wang Y, Shi X, Catani F, Ahmed B (2020b) Landslide characterization applying Sentinel-1 images and InSAR technique: the Muyubao landslide in the Three Gorges Reservoir Area China. *Remote Sens* 12(20):3385
- Zhou C, Yin K, Cao Y, Ahmed B (2016) Application of time series analysis and PSO-SVM model in predicting the Bazimen landslide in the Three Gorges Reservoir, China. *Eng Geol* 204:108–120
- Zhou C, Yin K, Cao Y, Ahmed B, Li Y, Catani F, Pourghasemi HR (2018a) Landslide susceptibility modeling applying machine learning methods: a case study from Longju in the Three Gorges Reservoir area, China. *Comput Geosci* 112:23–37
- Zhou C, Yin K, Cao Y, Intrieri E, Ahmed B, Catani F (2018b) Displacement prediction of step-like landslide by applying a novel kernel extreme learning machine method. *Landslides* 15(11):2211–2225
- Zhou J, Cui P, Yang X, Su Z, Guo X (2013) Debris flows introduced in landslide deposits under rainfall conditions: the case of Wenjiagou gully. *J Mt Sci* 10(2):249–260

### **Chao Zhou**

School of Geography and Information Engineering, China University of Geosciences, Wuhan 430078, China

### **Chao Zhou · Ying Cao · Kunlong Yin · Yue Wang**

Research Center of Geohazard Monitoring and Warning in the Three Gorges Reservoir, Chongqing 40400, China  
Email: yinkl@126.com

### **Ying Cao · Kunlong Yin (✉) · Yue Wang**

Faculty of Engineering, China University of Geosciences, Wuhan 430074, China  
Email: yinkl@126.com

### **Xie Hu**

College of Urban and Environmental Sciences, Peking University, Beijing 100871, China

### **Filippo Catani**

Department of Geosciences, University of Padova, Via Gradenigo 6, 35131 Padova, Italy